Journal of Applied Fluid Mechanics, Vol. 16, No. 4, pp. 750-764, 2023.
Available online at www.jafmonline.net, ISSN 1735-3572, EISSN 1735-3645.
https://doi.org/10.47176/jafm.16.04.1586

Effect of a Secondary Injection on the Performance of Three-Dimensional Over-under TBCC Exhaust Nozzles

H. Yang[1†], Q. Yang[1, 2], Z. Mu[2], Y. Shi[1] and L. Chen[1]

[1] *School of Power and Energy, Northwestern Polytechnical University, Xi'an, Shaan Xi Province, 710129, China*
[2] *Science and Technology on Scramjet Laboratory, CARDC, Sichuan, Mianyang, Si Chuan Province, 621000, China*

†*Corresponding Author Email: skylocust@mail.nwpu.edu.cn*

(Received October 1, 2022; accepted November 28, 2022)

ABSTRACT

A numerical simulation is used to investigate the flow field characteristics of a three-dimensional over-under turbine-based combined cycle circular-to-rectangular transition exhaust nozzle when only the turbojet flowpath is in operation. The effect on the exhaust nozzle performance of there being a secondary injection on the ramp of the expansion section of the turbojet flow path is then examined. Finally, the impact of variations in the secondary injection design parameters is further investigated. The results show that a secondary injection can improve the exhaust nozzle's performance by reducing the axial force on the inner wall of the flow path. However, changes in flight status can undermine this improvement. Under the baseline operating condition, a secondary injection with a larger angle and close to the ramp outlet can produce a more significant improvement in nozzle performance. In this study, the axial thrust coefficient, lift and pitch moment of the nozzle can be improved by a maximum of 9.312%, 66.007% and 10.975%, respectively.

Keywords: Three-dimensional over-under TBCC exhaust nozzle; Secondary injection; Flow control; Nozzle performance; Asymmetric expansion nozzle.

NOMENCLATURE

$A_{inlet,x}$	component of nozzle inlet area in the x-direction,
C_{fx}	axial thrust coefficient
F_s	ideal exhaust nozzle thrust
H	flight altitude
H_b	maximum throat height of turbojet flowpath
H_{base}	throat height of turbojet flowpath
I_{ex}	excess impulse at the nozzle outlet
l	length of nozzle
L	lift of nozzle
L_b	length of turbojet flowpath expansion section in the x-direction
L_{sec}	distance in the x-direction from the secondary injection inlet to the throat of the turbojet flowpath
M	nozzle pitch moment
Ma_∞	freestream Mach number
NPR	nozzle pressure ratio
R	gas constant
R_x	x-directional component of the relative pressure and viscous force integral on the inner wall surface of the nozzle
$R_{x,TFC}$	R_x of turbojet flowpath components
$R_{x,SFC}$	R_x of scramjet flowpath components
SPR	secondary injection pressure ratio
T_t	total temperature
$V_{inlet,x}$	x-directional component of nozzle inlet velocity
W_b	turbojet flowpath throat width
W_{sec}	secondary injection width
$\dot{m}_{inlet}$	mass flow rate at the nozzle inlet
$\dot{m}_{sec}$	secondary injection mass flow rate
$\dot{m}_{pri}$	mainstream mass flow rate
p_{amb}	ambient pressure
p_{inlet}	nozzle inlet pressure
p_t	total pressure
$p_{t,pri}$	mainstream total pressure
$p_{t,sec}$	secondary injection total pressure
w_{sec}	x-direction length of secondary injection outlet
x	x-direction coordinate
x_r	x-coordinate of point on the ramp
x_t	x-coordinate of the throat
y	y-direction coordinate
z	z-direction coordinate
γ	specific heat ratio
θ	incident angle of secondary injection
μ	viscosity coefficient
τ	wall shear stress

1. INTRODUCTION

Over-under turbine-based combined cycle (TBCC) exhaust nozzles have recently attracted attention because of their high specific impulse, wide flight envelope, and reusability. Their scramjet flow paths generally use a single expansion ramp nozzle (SERN) with a rectangular inlet and outlet, so as to more easily integrate with various aircraft. However, scramjet engines with circular or elliptical combustion chambers are increasingly considered superior (Melvin and Adam 2006; Siebenhaar and Bogar 2006). Many hypersonic vehicles with rectangular-shaped fuselages use these scramjet engines for their power systems (Walker *et al.* 2008; Melvin and Adam 2011). In this case, SERNs, which have rectangular inlets and outlets, do not fit the airframe very well. Various three-dimensional (3D) geometrical designs for asymmetric expansion nozzles with different inlet and outlet shapes have therefore been proposed (Lv *et al.* 2017a; Lu *et al.* 2010; Lv *et al.* 2017c). Importantly, this makes the throat adjustment scheme very different from typical splitter flap adjustment schemes.

Over-under TBCC exhaust nozzles mostly operate in cruise conditions, with the scramjet flowpath operating on its own. When it switches to the turbojet flowpath working on its own, the operating conditions for the entire exhaust nozzle are significantly outside the assumed design conditions. This leads to over-expansion inside the nozzle and a severe reduction in exhaust nozzle performance.

A number of studies have explored how to improve the performance of combined exhaust nozzles for off-design conditions. They generally approach this using either geometric adjustment methods or flow control methods. Geometric adjustment methods were applied earlier (Lederer 1996; Zhang *et al.* 2013) because they offer an easier way to change the flow structure inside the nozzle. However, they increase the complexity and weight of the nozzle's mechanical structure and reduce its operational reliability. Flow control techniques offer various active and passive flow control measures (Gronland and Berens 1995; Asbury *et al.* 1996; Tsunoda *et al.* 2000; Gamble and Haid 2004; Hao and Wang 2009; Zhou *et al.* 2016; Zhou and Wang 2019), with secondary injection and synthetic jet actuators (SJA) being the most-used active measures. Lv *et al.* (2017b) performed numerical simulations using a two-dimensional (2D) SERN model with cowl-based secondary injection. They explored the impact of different secondary injection parameters on exhaust nozzle performance and found that secondary injection can increase the thrust coefficient, lift and pitch moment of over-expanded SERNs by 3.16%, 29.43%, and 41.67%, respectively. Xu *et al.* (2010) investigated the impact of an SJA on over-expanded SERN performance. SJAs regularly "suck" and "puff" the flow near the wall under operating conditions, which can improve the whole SERN working cycle.

Although active and passive flow control techniques can improve the performance of combined exhaust nozzles, the focus this far has been primarily on SERNs with rectangular inlets and outlets, with flow control measures being implemented on splitter flaps or cowls. Over-under TBCC exhaust nozzles with different inlet and outlet shapes for the scramjet flowpath have a unique throat adjustment and significant 3D flow effects that have not yet been fully explored.

This paper looks at an over-under TBCC exhaust nozzle with a 3D circular-to-rectangular transition nozzle forming the scramjet flowpath. First, a numerical simulation of the flow field structure and performance under off-design conditions is presented. The impact of secondary injection on the performance is then investigated. Finally, the effect of different design parameters on the secondary injection flow is explored. This paper can serve as reference for the future exploration of how to improve over-under TBCC exhaust nozzles with different-shaped inlet and outlet scramjet flowpaths.

2. MODEL AND PARAMETERS

2.1 Geometric Model

In this study, a 3D asymmetric expansion nozzle with a circular inlet and a rectangular outlet is used for the scramjet flowpath in an over-under TBCC exhaust nozzle. A rotatable cowl and fixed shape-preserving plate are located at the bottom of the path outlet. A turbojet flowpath is mounted above the scramjet flowpath. Part of the upper expansion surface of the scramjet flowpath is shared between the two flowpaths (see Fig. 1).

It is difficult to avoid leakage by using a splitter flap for the throat adjustment because the upper expansion surface of the scramjet flowpath has a complex 3D shape. Previous throat adjustment

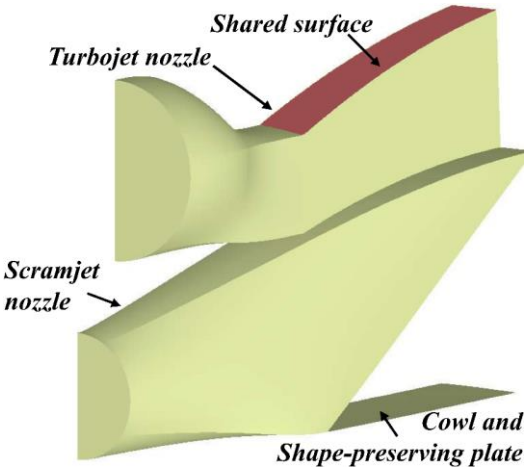

Fig. 1. Movable parts in the 3D over-under TBCC exhaust nozzle and the relationship between the two nozzles.

schemes for 3D over-under TBCC exhaust nozzles (e.g., Hua and Xu 2018) have suggested realizing throat adjustment through a combination of rotation

and sliding or rotation around the posterior axis (Xu *et al.* 2017). Here, the throat height of the turbojet flow path is adjusted using a combination of pre-rotation and sliding when the turbojet flowpath is operating on its own or undergoing modal transition. This scheme only rotates the shared surface at the beginning and end of each modal transition. The sliding of the shared surface is achieved by using two slide rails. The shared surface is rotated by means of the drive mechanisms on the two slide rails running at different speeds.

The following explains the adjustment process in detail. Ma_∞=0~3 is the stage where the turbojet flowpath is operating on its own. During this stage, the scramjet flowpath is kept closed. The throat height of the turbojet flowpath varies with the flight state (see Fig. 2(a)). Ma_∞=3~3.5 is the stage where modal transition occurs. Here, the turbine is gradually shut down and the flow in the turbojet flowpath decreases. The scramjet engine now starts, and the cowl gradually opens (see Fig. 2(b)). Ma_∞=3.5~6 is the stage where the scramjet flowpath is operating on its own. Here, the turbine runner is kept closed (see Fig. 2(c)).

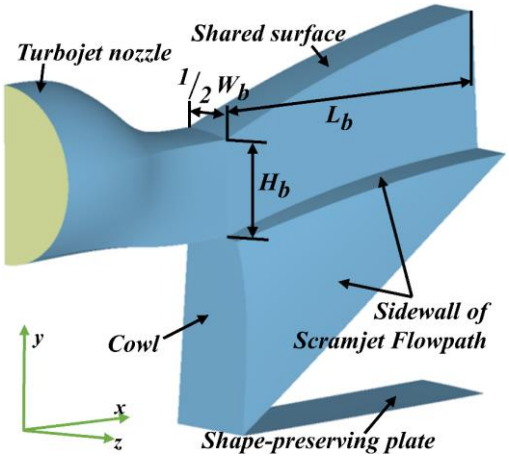

Fig. 3. Baseline nozzle at Ma_∞=0.8.

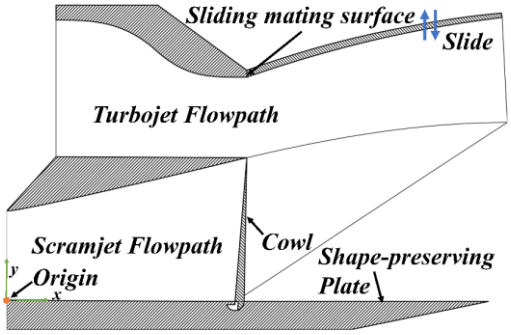

(a) Only the turbojet flowpath in operation

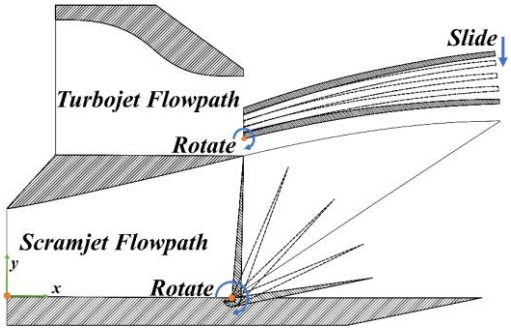

(b) Modal transition

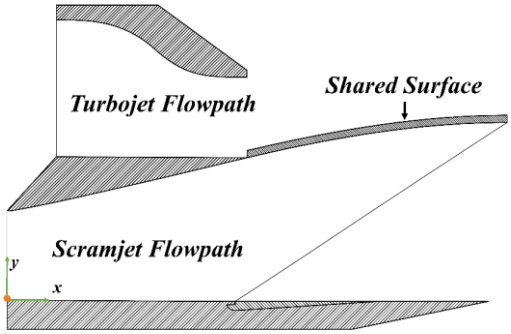

(c) Only the scramjet flowpath in operation

Fig. 2. Different working states of a 3D over-under TBCC exhaust nozzle.

During cruise conditions, there is no severe flow separation in the nozzle while the scramjet flowpath is working on its own. However, there is significant over-expansion and flow separation in the turbojet flowpath when the conditions are far from the designed-for condition. This situation is the focus of this paper.

This study treats a nozzle without flow control measures as a baseline nozzle here. Its baseline operating condition is Ma_∞=0.8. A model of this is shown in Fig. 3, where: W_b is the throat width of the turbojet flowpath in the baseline nozzle; L_b is the x-direction length of its expansion surface; and H_b is the maximum throat height of the turbojet flowpath. The cowl, shape-preserving plate, and scramjet sidewall collectively form the scramjet flowpath component (SFC), while the remainder forms the turbojet flowpath component (TFC). The study set out to explore whether a secondary injection could improve performance under off-design conditions.

The secondary injection takes place on the shared surface (see Fig. 4), where L_{sec}, w_{sec}, and θ are the three main geometric parameters of the secondary injection, representing the x-direction distance from the secondary injection inlet to the turbojet flowpath throat, the x-direction dimension of the secondary injection outlet, and the secondary injection incident angle, respectively. W_{sec} is the width of the secondary injection inlet, which is fixed at 0.75W_b.

2.2 Performance Parameters

The performance of the three-dimensional parallel TBCC exhaust nozzle was evaluated using the axial thrust coefficient, lift, and pitch moment. The entire

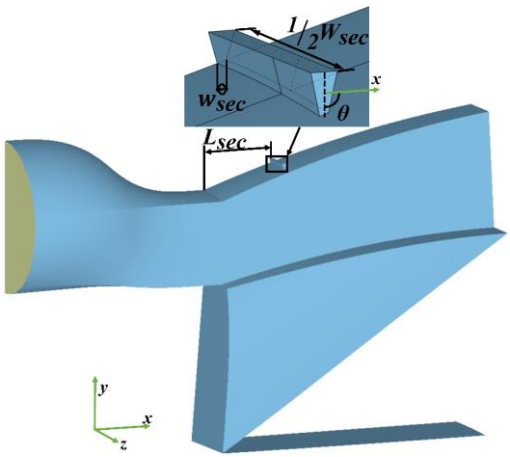

Fig. 4. Nozzle with secondary injection at Ma_∞=0.8.

inner wall of the exhaust nozzle was taken to be the control body for convenience. According to the law of conservation of momentum in an open system, the outlet excess impulse in the *x*-direction can be expressed as the difference between the inlet *x*-direction impulse and the *x*-direction component relating to the relative pressure and viscous force integral on the inner wall (Lv *et al.* 2017b). The excess impulse in the *x*-direction at the outlet of the exhaust nozzle can be solved using the following equation:

$$I_{ex} = \dot{m}_{inlet} V_{inlet,x} + \left(p_{inlet} - p_{amb}\right) A_{inlet,x} - R_x \tag{1}$$

where, $V_{inlet,x}$ and $A_{inlet,x}$ are the inlet velocity and inlet area components in the *x*-direction, respectively. R_x denotes the *x*-directional component for the relative pressure and viscous force integral on the inner wall of the nozzle. The surface of the exhaust nozzle where the integration is implemented is shown in blue in Figs. 3 and 4.

The following equation can be used to calculate the ideal isentropic thrust:

$$F_s = \dot{m}\sqrt{\frac{2\gamma}{\gamma-1}RT_t\left[1-\left(\frac{p_{amb}}{p_t}\right)^{\frac{\gamma-1}{\gamma}}\right]} \tag{2}$$

As the baseline nozzle has no flow control measures, its axial thrust coefficient can be defined as follows:

$$C_{fx,without} = \frac{I_{ex,without}}{F_{s,pri}} \tag{3}$$

where, $I_{ex,without}$ is the excess impulse at the outlet of the exhaust nozzle when the turbojet flowpath is operating on its own. $F_{s,pri}$ is the ideal isentropic thrust under the same conditions.

For a nozzle with secondary injection, the axial thrust coefficient can be calculated as follows:

$$C_{fx,with} = \frac{I_{ex,with}}{F_{s,pri} + F_{s,sec}} \tag{4}$$

The lift, *L*, of the over-under TBCC exhaust nozzle is the *y*-directional component of the relative pressure and viscous force integral for the inner wall of the nozzle. The reference point for the pitch moment, *M*, is the center point of the bottom of the scramjet flowpath inlet (i.e., the origin of the coordinates) (see Fig. 2).

NPR denotes the mainstream nozzle pressure ratio and *SPR* denotes the secondary injection pressure ratio. These can be calculated as follows:

$$NPR = \frac{p_{t,sec}}{p_{amb}} \tag{5}$$

$$SPR = \frac{p_{t,sec}}{p_{t,pri}} \tag{6}$$

3. NUMERICAL VALIDATION

3.1 Governing Equations

Detailed flow fields for all the over-under TBCC exhaust nozzles in this study were obtained using the commercial software Fluent, drawing on density-based solvers, a 3D space, and steady-state simulations. Assuming that the flow is ideal and compressible, the flow field can be solved using implicit equations. A Green-Gaussian Cell-based scheme was used for the gradient and a second-order upwind scheme was used for the convection. Numerical simulations were performed using an RNG *k*-*ε* two-equation turbulence model, with a standard wall function being used to handle the flow field near the wall. The flow is controlled by continuity, momentum, and energy equations. As steady-state calculations are being used here, the continuity equation can be written as:

$$\nabla \cdot (\rho \boldsymbol{V}) = 0 \tag{7}$$

The momentum equation is:

$$\nabla \cdot (\rho \boldsymbol{V}\boldsymbol{V}) = -\nabla p + \nabla \cdot \tau_{ij} \tag{8}$$

where τ_{ij} is the viscous stress tensor, and the energy equation is:

$$p(\nabla \cdot \boldsymbol{V}) = \nabla \cdot (\lambda' \nabla T) + \nabla \cdot (\boldsymbol{V} \cdot \tau_{ij}) + \rho q' \tag{9}$$

where λ' is the thermal conductivity. The viscosity, μ, is:

$$\mu = \mu_l + \mu_t \tag{10}$$

The laminar viscosity, μ_l, can be calculated using Sutherland's law with three coefficients:

$$\mu_l = \mu_0 \left(\frac{T}{T_0} \right)^{3/2} \frac{T_0 + S}{T + S} \tag{11}$$

where, $\mu_0 = 1.716 \times 10^{-5}\,\mathrm{Pa \cdot s}$, $T_0 = 273.11\mathrm{K}$, and $S = 110.56\mathrm{K}$ are the reference viscosity, reference temperature and effective temperature, respectively.

The turbulent viscosity, μ_t , can be obtained from the RNG k-ε two-equation model, and can be defined as follows:

$$\mu_t = \rho C_\mu \frac{k^2}{\varepsilon} \tag{12}$$

where k and ε are the turbulent kinetic energy and turbulent energy dissipation rate, respectively. $C_\mu = 0.0845$ is a constant.

3.2 Numerical Validation

The turbulence model was validated by comparing the calculated results with experimental data provided Waithe and Deere (2003). The latter performed thrust vectorization by using secondary injection in a convergent-divergent nozzle, resulting in a flow field structure that is similar to the one presented here. The reliability of the simulations can be more intuitively appreciated by comparing the calculated flow field structure with the Schlieren photographs given in Waithe and Deere (2003).

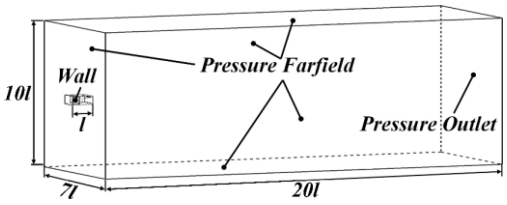

(a) The computational domain and boundary conditions

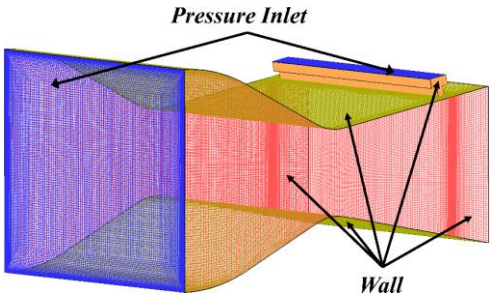

(b) Nozzle model with secondary injection, mesh, and boundary conditions

Fig. 5. Geometry, mesh and boundary conditions used for verification.

The geometric model, mesh, and boundary conditions used for turbulence model are shown in Fig. 5, where the secondary injection is placed in the expansion section. The aerodynamic boundary conditions were consistent with the experimental data, i.e., *NPR*=4.6, *SPR*=0.7. A 3D structured mesh of the flow field was divided using ICEM. The mesh near the nozzle walls was refined to meet the requirements of the turbulence model and standard wall function.

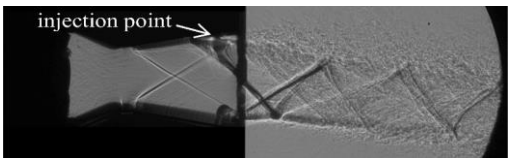

(a) Experimentally-based Schlieren photograph from Waithe and Deere (2003)

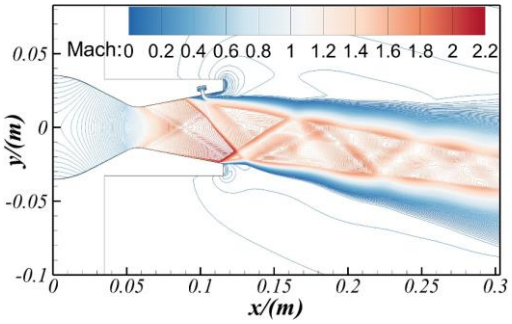

(b) Numerical simulation of Mach number contour

Fig. 6. Comparison of flow field structure in the plane of symmetry for numerical simulation and experiment results from Waithe and Deere (2003).

A comparison between the Mach number contour in the plane of symmetry obtained by the numerical simulation and an experimental Schlieren figure from Waithe and Deere (2003) is shown in Fig. 6. Figure 7 shows a detailed comparison of the experimental and calculated results for the centerline static pressure at the wall of the expansion section. It can be seen that there is a close match for the flow field structure in both images in Fig. 6(a). This confirms that numerical simulation is an effective

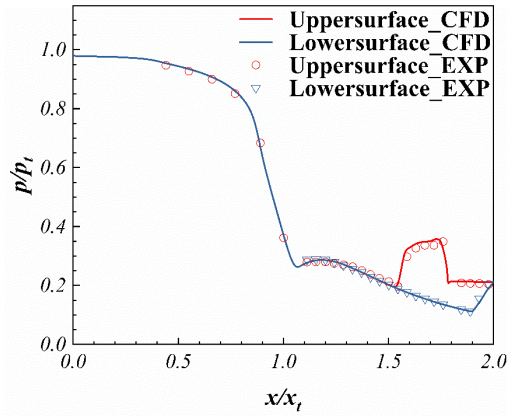

Fig. 7. Comparison of simulation and experimentally acquired pressure distribution on the centerline of the wall.

way of capturing the flow field details. The static pressure at the wall centerline obtained through the simulation also agrees well with the experimental results. On this basis, the RNG k-ε turbulence model with a standard wall function was used in this study.

3.3 Mesh Validation

ICEM was used to divide the structural mesh for the computational domain relating to both the baseline nozzle and the secondary injection nozzle. Figure 8 shows the divided mesh and boundary conditions. The resulting calculation domain was about $15L_b \times 10.5W_b \times 35W_b$, which was sufficient to avoid the far-field boundary having any influence on the calculation results. The mesh near the secondary injection nozzle outlet and the nozzle wall was refined. The height of the first mesh layer was set at 0.05mm to ensure that y^+ was between 30 and 60 and met the requirements of the wall function.

Mesh validation was performed on a baseline nozzle with the following three meshes: 1,935,127 (coarse); 3,847,171 (medium); and 7,736,663 (fine). The aerodynamic and geometric parameters used for the

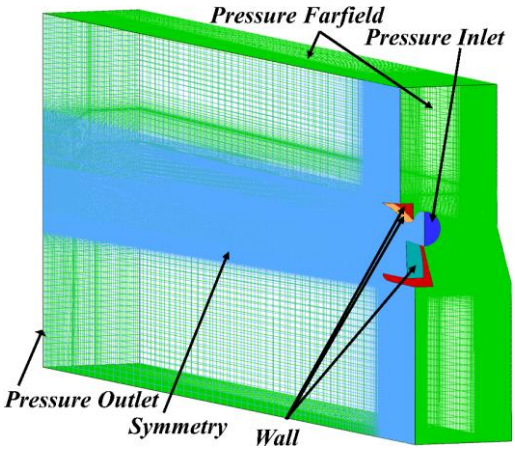

(a) Baseline nozzle

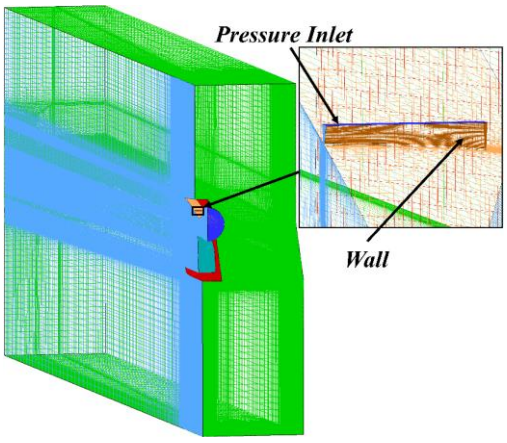

(b) Secondary injection nozzle

Fig. 8. Mesh and boundary conditions.

Table 1 Aerodynamic and geometric parameters for different types of nozzles under baseline operating condition

Parameter	Model	
	Baseline nozzle	Secondary injection nozzle
Ma_∞	0.8	0.8
H/km	5	5
NPR	3.793	3.793
SPR	/	1
T_t/K	2150	2150
H_b	H_b	H_b

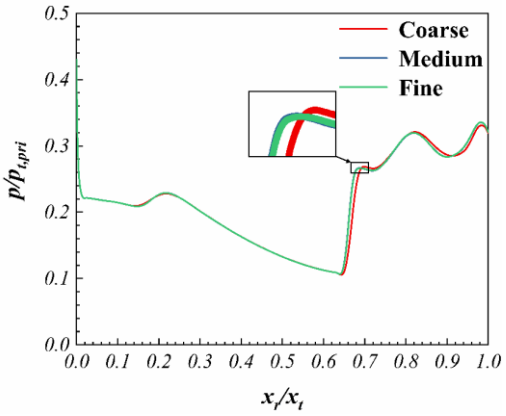

Fig. 9. Pressure distribution on the centerline of the ramp for different meshes.

numerical simulation are given in Table 1, and the validation results are shown in Fig. 9. The results for the pressure distribution on the centerline of the shared surface obtained using the medium and fine mesh were very close. However, the coarse mesh generated a slightly different pressure distribution and separation points. A mesh of not less than 3847171 cells was therefore used for the subsequent research. The mesh for the secondary injection nozzle was locally encrypted so that the flow field could be established at a reasonable computational cost.

4. RESULTS AND DISCUSSION

4.1 Flow Features

4.1.1 Performance of the Baseline Nozzle at Different Flight Mach Numbers

First, the flow of the baseline nozzle under several typical operating conditions was simulated. The flow field structure and performance parameters at Ma_∞=0.29 (takeoff), Ma_∞=0.8 (maximum throat height), Ma_∞=0.9 (minimum throat height), and Ma_∞=3 (maximum flight Mach number for just the turbojet flow path) were obtained. The parameters for typical operating conditions other than the baseline operating condition are shown in Table 2.

Figure 10 shows the Mach number contours in the nozzle's plane of symmetry for each operating condition. The flow inside the turbine runner was

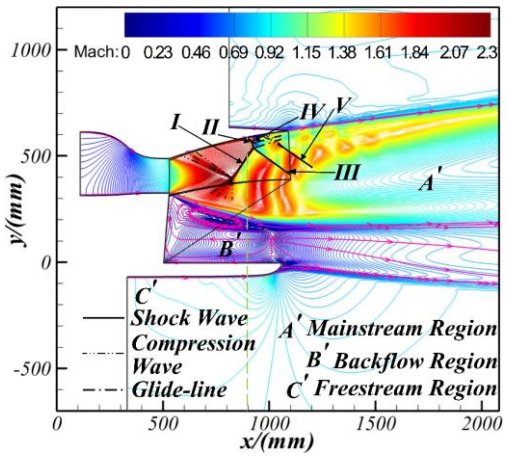

(a) Ma_∞=0.8

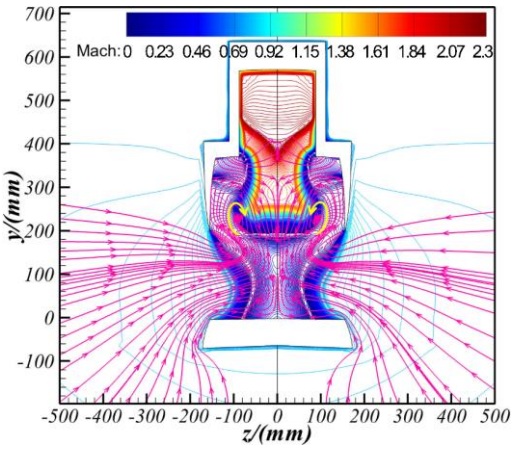

(b) Cross-section at 0.5L_b from the throat in the *x*-direction when Ma_∞=0.8

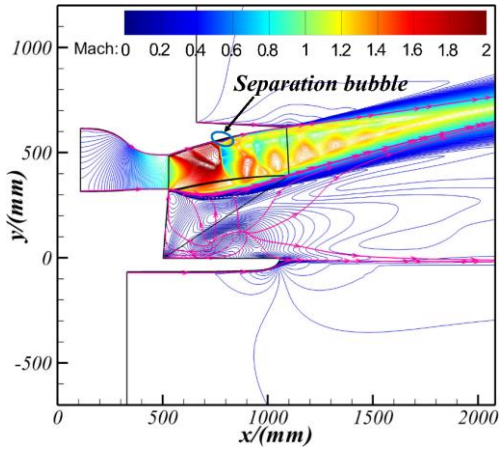

(c) Ma_∞=0.2

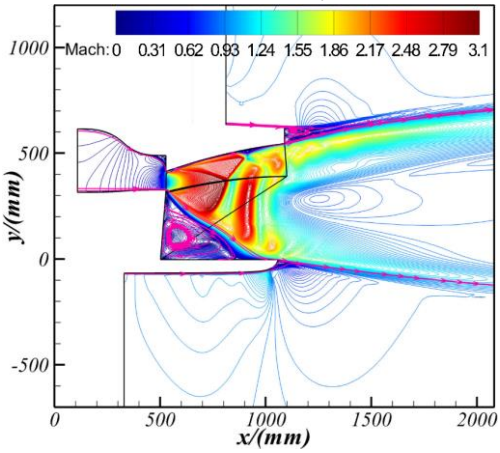

(d) Ma_∞=0.9

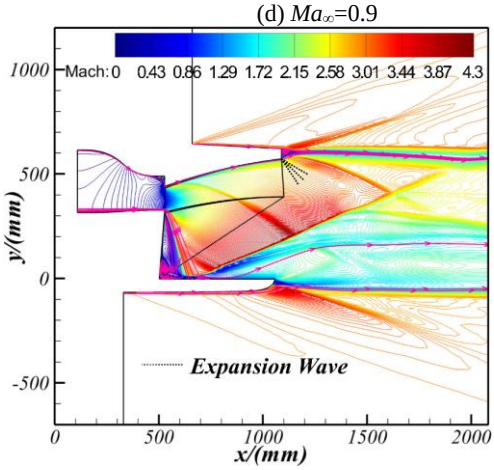

(e) Ma_∞=3

Fig. 10. Flow field structure of the over-under TBCC exhaust nozzle under different operating conditions.

heavily over-expanded for Ma_∞=0.29, 0.8, and 0.9. The actual flow structure inside the exhaust nozzle was similar under these three operating conditions, so analysis focused on the flow field structure in the baseline operating condition.

As shown in Fig. 10(a), the flow can be divided into a mainstream region, a free stream region, and a backflow region near the cowl. Interference from the shockwave and boundary layer in the flow path created a separation bubble in the rear section of the ramp. The mainstream flowed through this bubble

Table 2 Baseline nozzle parameters for various typical operating conditions

Parameters	Model		
	Baseline nozzle		
Ma_∞	0.29	0.9	3
H/km	0	11	18
NPR	2.615	8.018	30.194
SPR	/	/	/
T_t/K	2150	2138	2135
H_{base}	0.996H_b	0.539H_b	0.701H_b

and attached to the shared surface, forming a restricted shockwave separation structure. A smaller "λ" shockwave structure was formed by shockwaves *II* and *IV*, while a larger "λ" shockwave structure was formed by shock waves *I* and *III*. There was a Mach stem between these two "λ" shockwave structures and a series of compression waves were formed by the reduced curvature of the wall in front of shock wave *I*. These compression waves converged in the mainstream to form another shockwave. Another shockwave was generated by the convergence of the compression waves near the reattachment point of the separation bubble, i.e., shockwave *V*. Alternating shockwaves and expansion waves occurred after the mainstream crossed shockwaves *I, III* and *V*. This wave system gradually disappeared as the mainstream and freestream began to mix.

However, the flow in the backflow region was affected by both mainstream and freestream suction effects. As the Mach number increased from Ma_∞=0.29 to Ma_∞=3, the suction effect became stronger, resulting in a smaller backflow region and more of the mainstream entering the cavity made up of the scramjet flowpath components. As can be seen in Fig. 10(a), there was a focal point and a knot in the backflow region. Figure 10(b) shows the vortex structure present in the backflow region. This vortex slowly pushed the mainstream towards the downstream shape-preserving plate. However, at the same time, the spanwise size of the middle and lower part of the mainstream gradually decreased. Eventually, the high-speed zone in the mainstream was divided into an upper and lower part, with a central part containing a mixed flow.

At Ma_∞=3, the mainstream was under-expanded in the expansion section of the turbojet flowpath. The suction effect from the freestream and mainstream reduced the area of the backflow region to almost nothing and the mainstream came close to touching the shape-preserving plate. A strong shock wave was ultimately generated when the mainstream over-expanded above the shape-preserving plate. Although the turbojet flowpath was under-expanded in this condition, the over-under TBCC exhaust nozzle as a whole was still over-expanded.

Mach number-related variations in the performance parameters of the over-under TBCC exhaust nozzle with the turbojet flowpath operating on its own are shown in Fig. 11. In Fig. 11(a), it can be seen from the axial thrust coefficient curve that the C_{fx} of the exhaust nozzle initially decreased, then increased as the freestream Mach number increased. The C_{fx} of the exhaust nozzle was 0.816 at Ma_∞=0.29. Over-expansion of the mainstream occurred only inside the turbojet flowpath, while the flow inside the backflow region was less affected. The difference between the flow pressure in the backflow region and the ambient pressure was minimal, so the drag generated in the backflow region had little effect on the exhaust nozzle's performance. At Ma_∞=0.8, the over-expansion of the mainstream began to weaken. However, the flow in the backflow region suffered a greater pressure loss as a result of the suction. The

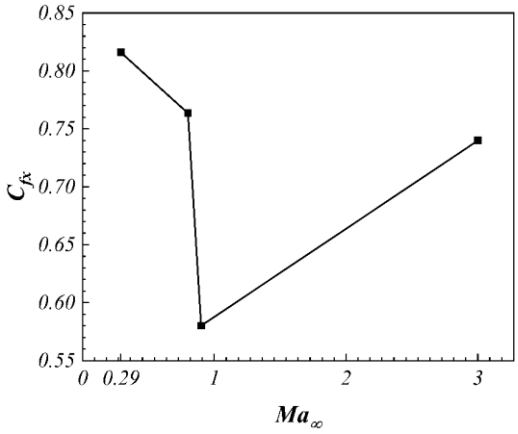

(a) Axial thrust coefficient

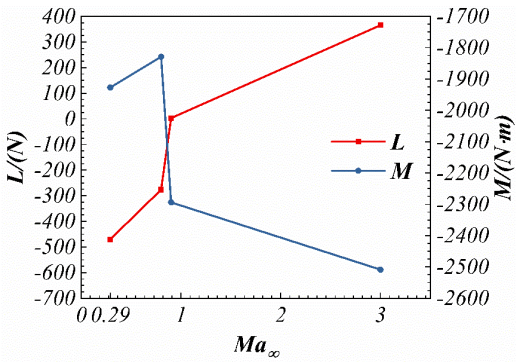

(b) Lift and pitch moment

Fig. 11. Performance parameters for different operating conditions.

differential pressure drag generated by the backflow region at this point reduced the C_{fx} of the exhaust nozzle to 0.7635. At Ma_∞=0.9, the over-expansion of the mainstream became stronger. The flow in the backflow area was further impacted by the suction and the mainstream was forced to expand, producing a powerful shockwave. At this point, the height of the throat of the turbojet flowpath was at its lowest and a significant backflow was generated in front of the throat. All these factors had a negative impact on the C_{fx}, bringing it down to just 0.5801. At Ma_∞=3, there was a strong shockwave caused by over-expansion in the backflow region. However, this shockwave was outside the nozzle, so it had little effect on the performance. Under-expansion in the turbojet flowpath and backflow-related drag were the main causes of thrust loss. After the loss of performance at Ma_∞=0.9, the C_{fx} rose again to 0.7399 at Ma_∞=3.

Figure 11(b) demonstrates the variations in the lift and pitch moment of the exhaust nozzle according to the flight Mach number. The lift gradually increased from -470.04N to 365.41N as the Mach number increased. The pitch moment was always negative, so that the exhaust nozzle remained head-up throughout the stage where the turbojet flowpath was operating on its own. The specific performance parameters for different flight Mach number conditions are shown in Table 3.

Table 3 Performance parameters of the over-under TBCC exhaust nozzle for typical operating conditions

Mach	C_{fx}	$L/(N)$	$M/(N·m)$
0.29	0.816	-470.04	-1927.23
0.8	0.7635	-276.56	-1828.93
0.9	0.5801	3.05	-2293.98
3	0.7399	365.41	-2508.59

4.1.2 Flow Field for the Secondary Injection Nozzle under Baseline Operating Conditions.

To improve the performance of the over-under TBCC exhaust nozzle when the turbojet flowpath is operating on its own, a secondary injection was introduced on the shared surface. The parameters relating to the secondary injection are given in Table 4. The Mach number contours in the plane of symmetry for the secondary injection exhaust nozzle at Ma_∞=0.8 are given in Fig. 12.

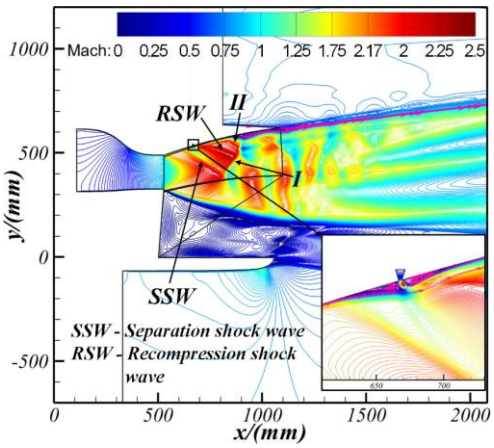

Fig. 12. Mach number contours for the secondary injection nozzle at Ma_∞=0.8.

Table 4 Secondary injection parameters

SPR	T_t/K	$\dot{m}_{sec}$	L_{sec}	θ/°	W_{sec}
1	300	3%	$0.25L_b$	90	$0.75W_b$

As shown in Fig. 12, the secondary injection was placed on the shared surface at $0.25L_b$ from the throat of the turbojet flowpath. A separate shockwave generated before the secondary injection then replaced the shockwave formed by the multiple compression waves in the baseline nozzle. A reattachment shockwave was generated behind the secondary injection that intersected with shockwave *I* downstream. Shockwave *II* moved slightly forward in this condition and the separation zone behind it expanded. The secondary injection also caused the separation zone behind shock wave *II* to move from being closed to open. The change in the location of the shockwaves due to the secondary injection also resulted in the Mach stem between shockwaves *I* and *II* moving slightly downward.

The flow field of the nozzle with a secondary injection was calculated under the same conditions as the baseline nozzle, so the sum of the first two terms on the right side of Eq. (1) remained equal. The only thing affecting the axial thrust's magnitude was therefore R_x. Figure 13 shows a comparison of $R_{x,TFC}$ and $R_{x,SFC}$ for exhaust nozzles with and without flow control measures. The results show that a secondary injection can reduce the $R_{x,TFC}$ and $R_{x,SFC}$ of the exhaust nozzle, significantly reducing its R_x as well.

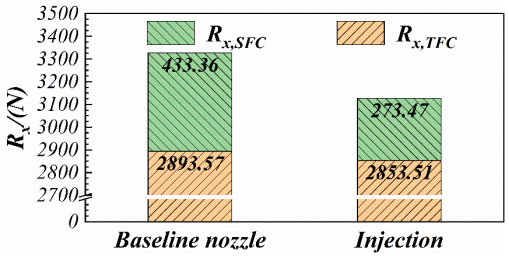

Fig. 13. Comparison of the *x*-directional components for the relative pressure and viscous force wall integral for exhaust nozzles with different flow control measures.

Table 5 shows the performance parameters of the different exhaust nozzles. The significant reduction in the R_x of the exhaust nozzle results in a substantial increase in the axial thrust coefficient, lift, and pitching moment. According to the above analysis, installing a secondary injection on the shared surface of an over-under TBCC exhaust nozzle can improve its performance. However, it is important to also assess the impact of different secondary injection parameters and flight Mach numbers on this performance improvement. This is discussed in section 4.2.

Table 5 Performance of the nozzles with and without flow control measures

	Baseline nozzle	Secondary injection nozzle
C_{fx}	0.7635	0.8203
L/(N)	-276.56	-250.64
M/(N·m)	-1828.93	-1747.69
ΔC_{fx}	/	7.439%
ΔL	/	9.372%
ΔM	/	4.442%

4.2 Effect of Different Parameters on the Flow Field and Performance of a Secondary Injection Nozzle

4.2.1 Mass Flow

The effect of the secondary injection's mass flow rate on the nozzle's performance was investigated first. The relevant mass flow rates were 3%, 4.51%, and 6.01% of the mainstream mass flow rate, i.e., $\dot{m}_{sec}$=0.03$\dot{m}_{pri}$, 0.0451$\dot{m}_{pri}$, and 0.0601$\dot{m}_{pri}$, respectively. The other parameters were kept constant for each of the different mass flow rates. Thus, the distance between the secondary injection and the throat was fixed at $0.25L_b$ and the injection

angle was fixed at 90°. The *SPR* was fixed at 1 and the operational condition was fixed at Ma_∞=0.8.

Figure 14 shows the Mach number contours of the flow field at $\dot{m}_{sec}$=0.0451$\dot{m}_{pri}$ and 0.0601$\dot{m}_{pri}$. The Mach contours for $\dot{m}_{sec}$=0.03$\dot{m}_{pri}$ were presented in Fig. 12. An increase in the secondary injection mass flow rate led to a gradual increase in the intensity of the separation shockwave and the extent of the upstream separation zone. The enlargement in the lower right corner of the image makes the difference in flow structure clearer. As the mass flow rate increased from 0.03$\dot{m}_{pri}$ to 0.0601$\dot{m}_{pri}$, the thickness of the backflow region downstream of the secondary injection also increased significantly. The backflow region also changed from being closed to open and the mainstream behind the secondary injection was no longer attached to the wall. The distance between the mainstream and the shared surface gradually increased downstream of the secondary injection and there was an overall tendency to move away from the shared surface.

The flow structure, such as the Mach stem and the "λ" shockwaves resulting from mainstream over-expansion, also changed as the secondary injection mass flow rate increased. For instance, there was a significant reduction in the length of the Mach rod in the mainstream. However, the separation shockwave emanating from the backflow region and the reattachment shockwave downstream of the secondary injection remained.

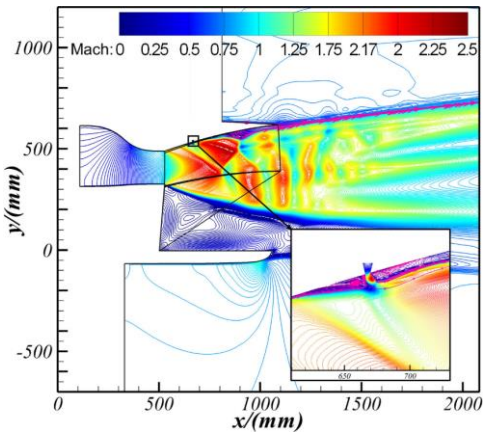

(a) $\dot{m}_{sec}$=4.51%

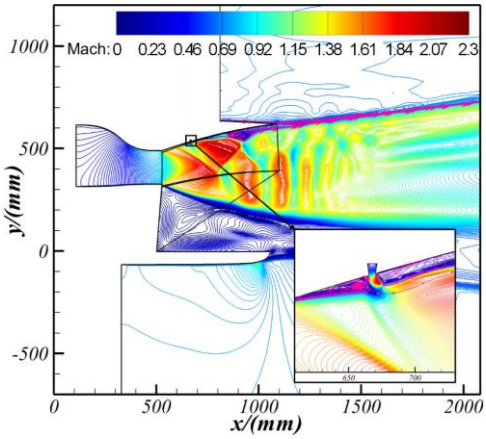

(b) $\dot{m}_{sec}$=6.01%

Fig. 14. Mach number contours in the exhaust nozzle's plane of symmetry for different mass flow rates.

Figure 15 reveals the impact of increasing the secondary injection mass flow rate on the R_x of the exhaust nozzle. First, it can be seen that an increase in the secondary injection mass flow rate did not always cause a decrease in R_x. The $R_{x,SFC}$ and $R_{x,TFC}$ of the exhaust nozzle slightly increased for $\dot{m}_{sec}$=0.0601$\dot{m}_{pri}$ when compared to $\dot{m}_{sec}$=0.0451$\dot{m}_{pri}$. Close examination of the Mach number contours reveals that the flow near the wall downstream of the secondary injection at $\dot{m}_{sec}$ =0.0601 $\dot{m}_{pri}$ had an elevated velocity before separation, potentially leading to a decrease in pressure at the nearby wall. However, while the extent of the separation zone and the intensity of the separation shockwave increased slightly upstream of the secondary injection, the benefits of the increased upstream wall pressure were somewhat offset by a decrease in the downstream wall pressure. The R_x of the exhaust nozzle ultimately ceased to decrease as the secondary injection flow rate increased.

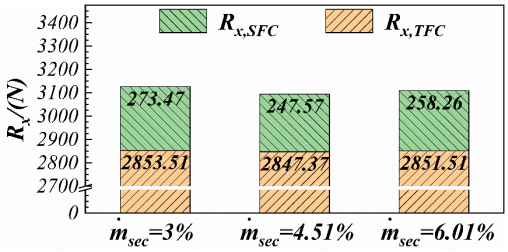

Fig. 15. Comparison of the *x*-directional components for the relative pressure and viscous force wall integral for exhaust nozzles with different mass flow rates.

Table 6 shows the performance parameters of the exhaust nozzle for different secondary injection flow rates. The results show that the different mass flow rates all improved the exhaust nozzle performance, given the fixed combination used in this study of L_{sec}, θ, and the flight Mach number. However, an increase in $\dot{m}_{sec}$ did not always improve the performance. The performance benefits started to decrease when the mass flow rate became too high. Although the R_x of the exhaust nozzle was slightly lower at

Table 6 Performance of the nozzle for different injection mass flow rates

	$\dot{m}_{sec}$		
	3%	4.51%	6.01%
C_{fx}	0.8203	0.8258	0.8159
L/(N)	-250.64	-236.1	-261.88
M/(N·m)	-1747.69	-1733.09	-1764.86
ΔC_{fx}	7.439%	8.16%	6.863%
ΔL	9.372%	14.63%	5.308%
ΔM	4.442%	5.24%	3.503%

$\dot{m}_{sec}$=0.0601$\dot{m}_{pri}$ than at $\dot{m}_{sec}$=0.03$\dot{m}_{pri}$, the larger mass flow rate resulted in a larger ideal isentropic thrust. Referring to Eq. (4), the ideal isentropic thrust of the whole exhaust nozzle increased as well. The axial thrust coefficient therefore decreased when the decrease in R_x was insufficient to offset the increase in the ideal isentropic thrust.

4.2.2 Injection Angle

Next, the effect of the secondary injection angle on the exhaust nozzle's performance was investigated. Three injection angles were assessed, θ=45°, 90°, and 135°. During this, the distance between the secondary injection and the throat was fixed at L_{sec}=0.25L_b. The injection mass flow rate was fixed at $\dot{m}_{sec}$=0.0451$\dot{m}_{pri}$, the *SPR* was fixed at 1, and the flight Mach number was fixed at Ma_∞=0.8.

Figure 16 shows the flow field Mach number contours for injection angles of θ=45° and 135°. The Mach number contours for θ=90° were already presented in Fig. 14(a). The results show that the effect of the secondary injection on the mainstream flow increased as the injection angle increased. The flow field structure near the secondary injection outlet at θ=45° was relatively close to that of θ=90°.

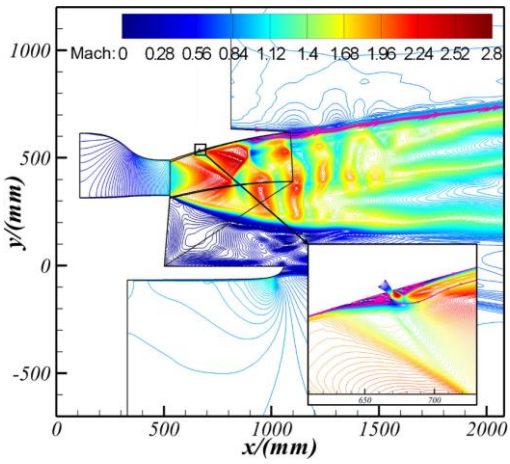

(a) θ=45°

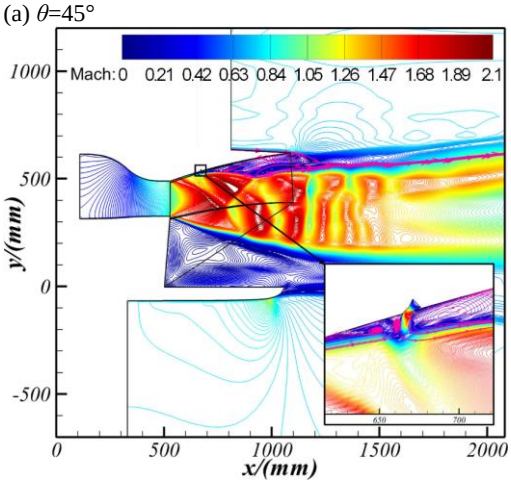

(b) θ=135°

Fig. 16. Mach number contours in the plane of symmetry for different injection angles.

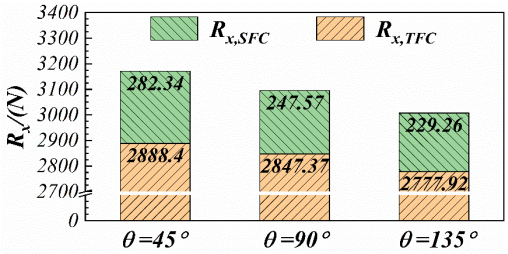

Fig. 17. Comparison of the *x*-directional components for the relative pressure and viscous force wall integral for different injection angles.

However, the separation shockwave angle upstream of the secondary injection increased slightly when θ=45° and the extent of the downstream backflow region was slightly reduced. At θ=135°, the direction of the secondary jet was opposite to that of the mainstream. This made the upstream separation zone increase significantly and the location of the separation shockwave moved forward. The mainstream was completely separated downstream of the secondary injection. There was more external flow between the mainstream and the shared surface, but no significant backflow region was formed.

The presence of a low-velocity external flow helped the pressure at the wall downstream of the secondary injection to increase. The separation zone upstream of the secondary injection that expanded as the injection angle increased was also effective in raising the pressure at the upstream wall. Thus, the R_x of the exhaust nozzle decreased as the injection angle increased (see Fig. 17).

The above analysis is supported by the performance parameters shown in Table 7. The axial thrust coefficient, lift, and pitch moment of the exhaust nozzle all improved as the secondary injection angle increased, with the exhaust nozzle lift improving the most. Thus, the angle between the direction of the secondary injection and the mainstream flow should be increased as much as possible when implementing a secondary injection on a shared upper expansion surface.

4.2.3 Injection Location

The effect of the location of the secondary injection on the exhaust nozzle's performance was also investigated. Three locations were chosen, L_{sec}=0.25L_b, 0.5L_b, and 0.75L_b. The mass flow rate was fixed at $\dot{m}_{sec}$=4.51%. The injection angle was fixed at θ=90°, the *SPR* was fixed at 1, and the flight Mach number was fixed at Ma_∞=0.8.

Table 7 Nozzle performance for different injection angles.

	θ		
	45°	90°	135°
C_{fx}	0.8207	0.8258	0.8346
L/(N)	-245.44	-236.1	-94.01
M/(N·m)	-1747.81	-1733.09	-1628.21
ΔC_{fx}	7.492%	8.16%	9.312%
ΔL	11.253%	14.63%	66.007%
ΔM	4.435%	5.24%	10.975%

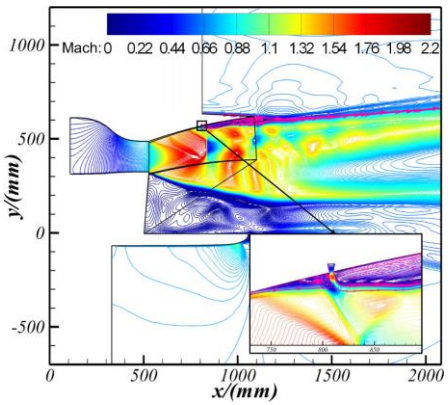

(a) L_{sec}=0.5L_b

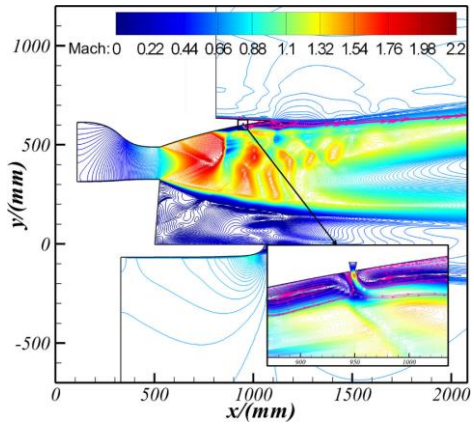

(b) L_{sec}=0.75L_b

Fig. 18. Mach number contours for different injection locations.

Figure 18 shows the Mach number contours for a secondary injection at 0.5L_b and 0.75L_b from the throat. The Mach number contours for a secondary injection at 0.25L_b from the throat were shown in Fig. 14(a). Changes to the location of the secondary injection had a significant impact on the flow structure of the mainstream. When L_{sec}=0.5L_b, the secondary injection was close to the upstream flow from shockwave *II* in the baseline nozzle. The shockwave upstream of the secondary injection was the direct reason why the mainstream was separated and contained a longer Mach stem. The mainstream was no longer attached to the shared surface downstream of the secondary injection. The external low-energy flow from the end of the shared surface and close to the wall turned and filled the cavity created by the mainstream separation, creating a backflow.

When L_{sec}=0.75L_b, the secondary injection was located downstream of shockwave *IV* in the baseline nozzle flow field. A separation shockwave appeared upstream of the secondary injection. The extent of the separation zone behind the separation shockwave was then increased and the mainstream separation point moved forward. Due to this change in the location of the separation shockwave, the locations of the Mach stem and the "λ" shockwave in the mainstream also moved forward significantly.

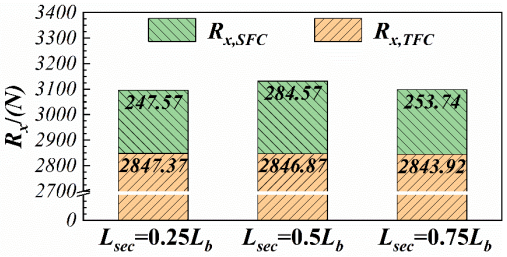

Fig. 19. Comparison of the *x*-directional components for the relative pressure and viscous force wall integral for different injection locations.

Table 8 Performance of the nozzle for different injection locations.

	L_{sec}		
	0.25L_b	0.5L_b	0.75L_b
C_{fx}	0.8258	0.8133	0.8276
L/(N)	-236.1	-261.33	-197.83
M/(N·m)	-1733.09	-1770.98	-1703.02
ΔC_{fx}	8.16%	6.523%	8.396%
ΔL	14.63%	5.507%	28.468%
ΔM	5.24%	3.169%	6.884%

Additionally, the mainstream was no longer attached to the shared surface downstream of the secondary injection.

The R_x of the exhaust nozzle for the different secondary injection locations is shown in Fig. 19 and the resulting performance parameters of the exhaust nozzle are given in Table 8. It can be seen that the $R_{x,TFC}$ gradually decreased as the position of the secondary injection moved backwards, while the $R_{x,SFC}$ initially increased and then decreased. The R_x of the exhaust nozzle was slightly larger when the secondary injection was at L_{sec}=0.75L_b than when it was at L_{sec}=0.25L_b. However, the secondary injection at L_{sec}=0.75L_b produced a more significant improvement in the exhaust nozzle performance. The lift of the exhaust nozzle was particularly improved. This was mainly because of the smaller isentropic thrust of the secondary injection at L_{sec}=0.75L_b. According to Eq. (4), with a small difference in the exhaust nozzle's $I_{ex,with}$, the smaller $F_{s,sec}$ will also reduce the denominator and may eventually lead to the axial thrust coefficient increasing instead. In summary, when $\dot{m}_{sec}$, θ and the flight Mach number have the fixed combination used in this study, a secondary injection can significantly improve the performance parameters of an over-under TBCC exhaust nozzle, regardless of where it is installed on the shared surface. However, positioning the secondary injection as close as possible to the exhaust nozzle outlet will maximize the improvements in the lift and pitch.

4.3 Effect of Different Flight Mach Numbers on the Flow Field and Performance

As the exhaust nozzle is subject to over-expansion under several operating conditions, the effects of different flight Mach numbers on the improvements

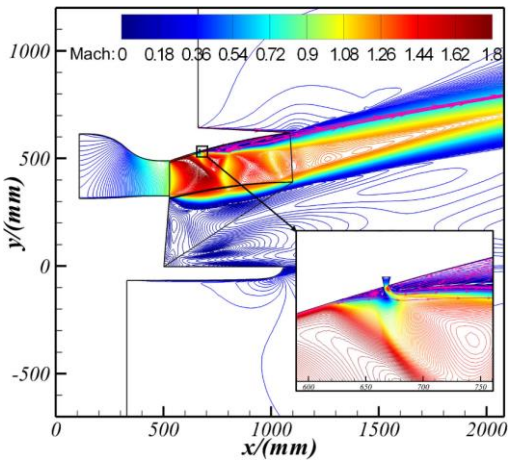

(a) Ma_∞=0.29

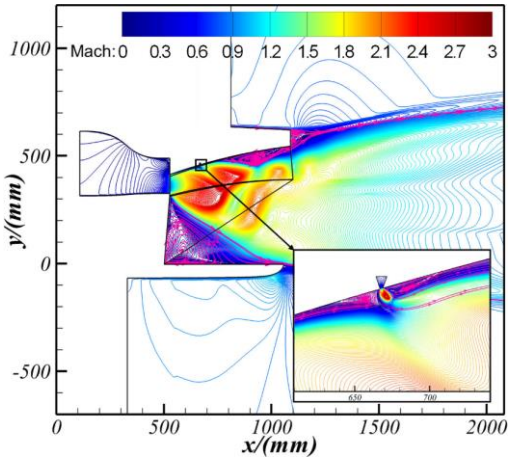

(b) Ma_∞=0.9

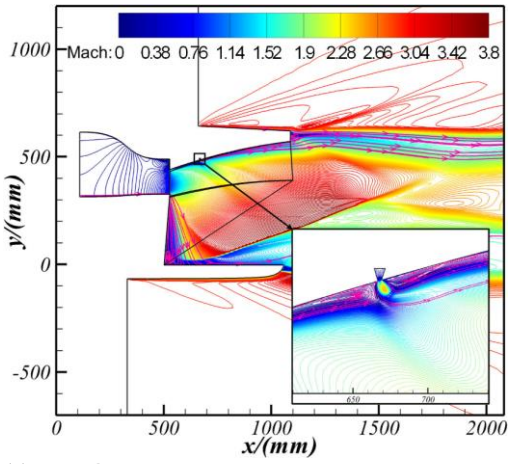

(c) Ma_∞=3

Fig. 20. Mach number contours for different flight Mach numbers.

deriving from having a secondary injection were also examined. Apart from the baseline operating condition, the effects were also investigated for Ma_∞=0.29, 0.9, and 3. The mass flow rate of the secondary injection was maintained at $\dot{m}_{sec}=0.0451\dot{m}_{pri}$, and the injection angle was fixed at θ=90°. The injection location was fixed at $L_{sec}=0.25L_b$, and the *SPR* was fixed at 1.

The resulting Mach number contours for the flow field under different flight conditions are shown in Fig. 20.

If Figs. 20(a) and 10(c) are compared, it can be seen that the secondary injection at Ma_∞=0.29 produced an earlier separation of the mainstream. It is clear from the streamlines that the separation was open, with the external flow turning down the wall and filling the region between the mainstream and the shared surface. Although the mainstream was completely separated downstream of the secondary injection, the location of its lower boundary did not change significantly. The flow area of the mainstream was therefore somewhat reduced and its over-expansion mitigated.

At Ma_∞=0.9, the secondary injection was significantly further from the mainstream separation point in the baseline nozzle. However, the backflow region downstream of the secondary injection prevented the mainstream from returning to the wall and, subsequently, the mainstream separated due to over-expansion. Thus, introducing a secondary injection resulted in a significantly larger separation zone compared to the flow field of the baseline nozzle, with the mainstream failing to reattach to the shared surface after separation. It should be noted, though, that the separation zone was closed and no external flow entered.

The interference of the secondary injection upon the mainstream was equally obvious at Ma_∞=3. Here, the thickness of the low-velocity zone upstream of the secondary injection exceeded the flow field at the same location for the baseline nozzle. In comparison, however, the reattachment shockwave at the back of the baseline nozzle throat tended to disappear. In addition, the thickness of the boundary layer of the mainstream downstream of the secondary injection increased significantly, such that the mainstream did not separate. The extent of the backflow region near the cowl was also further reduced by the secondary injection.

Figures 21 and 22 show a comparison between the R_x and exhaust nozzle performance parameters before and after the introduction of the secondary injection for different flight Mach numbers. The results show that introducing a secondary injection at Ma_∞=0.29

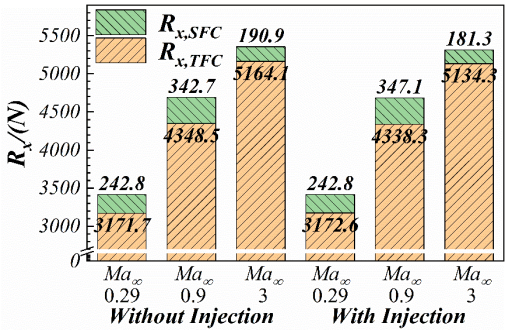

Fig. 21. Comparison of the *x*-directional components for the relative pressure and viscous force wall integral for different flight Mach numbers.

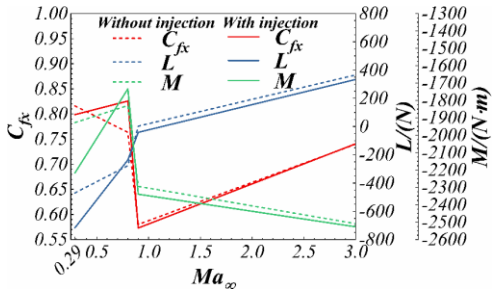

Fig. 22. Comparison of exhaust nozzle performance parameters before and after secondary injection at different flight Mach numbers.

did not significantly change the $R_{x,TFC}$ and $R_{x,SFC}$. The pressure of the low-velocity fluid in the separation zone downstream of the secondary injection was lost due to viscous dissipation. This made the wall pressure of the shared surface downstream of the secondary injection lower than that of the baseline nozzle. The pressure rise caused by the separation shockwave upstream of the secondary injection was insufficient to offset this negative effect and the R_x of the exhaust nozzle did not change significantly. The effect of the secondary flow's isentropic thrust also needs to be considered when calculating the axial thrust coefficient after introducing a secondary injection. If there is no significant change in the R_x, there will inevitably be a decrease in the axial thrust coefficient. In addition, the use of a secondary injection also needs to reduce the lift and pitch moment of the exhaust nozzle.

At Ma_∞=0.9, the $R_{x,TFC}$ of the exhaust nozzle slightly decreased and the $R_{x,SFC}$ slightly increased after the introduction of the secondary injection. The R_x was slightly lower than that of the baseline nozzle. The secondary injection increased the extent of the backflow region in the mainstream at the rear of the shared surface. This enhanced the fluid interaction inside the backflow region, which in turn increased the viscous dissipation, resulting in a lower static pressure in the backflow region. However, the pressure rise caused by the separation shockwave upstream of the secondary injection somewhat offset this adverse effect, such that the $R_{x,TFC}$ was ultimately slightly lower than that of the baseline nozzle. Nevertheless, the difference in the R_x of the exhaust nozzle before and after the secondary injection's introduction was insignificant. Overall, the axial thrust coefficient decreased once the secondary injection's isentropic thrust is taken into account.

At Ma_∞=3, the $R_{x,SFC}$ and $R_{x,TFC}$ of the exhaust nozzle both slightly reduced after introduction of the secondary injection. A more significant reduction in the R_x under this condition led to the axial thrust coefficient being slightly higher than that of the baseline nozzle. Ultimately, across all three flight Mach number conditions, introducing a secondary injection caused a decrease in the lift and pitch moment.

The above analysis has shown that a variety of different secondary injection angles and locations will all improve the performance of an over-under TBCC exhaust nozzle under baseline operating conditions. Up to a certain point, when using a secondary injection, the mass flow rate increased sufficiently to improve the performance of the exhaust nozzle. However, beyond a certain value, this performance gain starts to decline. When the secondary injection is installed close to the throat, the performance is strongly affected by the flight Mach number. In practice, it is best for the secondary injection to be mounted with a large injection angle near the end of the shared surface to maximize its positive impact.

5. CONCLUSION

This study has analyzed the 3D flow field characteristics and performance of an over-under TBCC exhaust nozzle when only the turbojet flowpath is in operation. The impact of installing a secondary injection on the performance of the exhaust nozzle when operating outside of designed-for condition was also investigated. In addition, the influence of different secondary injection parameters on the flow control effect was explored. The study gives rise to the following conclusions：

(1) When the turbojet flowpath is working on its own and over-expanded, the flow inside the backflow region formed by the closed scramjet flowpath is affected by a suction effect that increases with the flight Mach number. This suction shifts the main flow in the turbojet flowpath lower, into the scramjet flow path. The low-velocity flow in the backflow region then forces the mainstream to move toward the plane of symmetry, with it ultimately splitting into multiple jets.

(2) A secondary injection causes mainstream separation both upstream and downstream of the point of injection. This increases the wall pressure and reduces the axial force on the inner wall of the exhaust nozzle, thus improving the axial thrust coefficient, the lift, and the pitch moment. However, as the position of the shared surface is not fixed, the performance improvement produced by the secondary injection is heavily dependent upon changes in the flight conditions.

(3) Under baseline operating conditions, a secondary injection can significantly improve the performance of an over-under TBCC exhaust nozzle. The larger the injection angle and the closer the installation to the outlet the better the performance outcome. A secondary injection can increase the axial thrust coefficient, lift, and pitch moment by up to 9.312%, 66.007%, and 10.975%, respectively. Assessment of the influence of different parameters has suggested that when using a secondary injection in practice, a moderate mass flow rate, large injection angle, and position as close to the outlet as possible will result in the most satisfactory improvement of the axial thrust coefficient, lift, and pitch moment.

Using a secondary injection to improve the performance of an over-under TBCC exhaust nozzle with a differently shaped inlet and outlet for the

scramjet flowpath has proved to be both feasible and effective. This is especially the case for off-design operating conditions. However, the fixed geometric and aerodynamic parameters of the secondary injection mean that it does not always improve the performance of the exhaust system when the flight conditions change. There is therefore a need to further explore the influence of the flight conditions on the performance of secondary injections in future work, so as to ensure a consistent improvement in nozzle performance.

ACKNOWLEDGEMENTS

We would like to acknowledge the support of the Science and Technology on Scramjet Laboratory (grant number STSMY-KFKT-2020002). The authors would also like to express their thanks to the editors and reviewers of this paper.

REFERENCES

Asbury, S. C., C. L. Gunther and C. A. Hunter (1996). A passive cavity concept for improving the off-design performance of fixed geometry nozzles. *AIAA Paper* 96-2541.

Gamble, E. J. and D. Haid (2004). Improving off-design nozzle performance using fluidic injection. *AIAA Paper* 1206.

Gronland, T. A. and T. M. Berens (1995). Nozzle/afterbody integration for hypersonic vehicle by means of secondary air injection. *AIAA Paper* 95-6050.

Hao, D. X. and Z. X. Wang (2009). The design and flow field simulation of single expansion ramp nozzle with variable flaps. *Machinery Design & Manufacture* 12, 8-10 (in Chinese).

Hua, W. D. and J. L. Xu (2018). Design approach and experiment of three-dimensional over/under TBCC exhaust system. *Journal of Aerospace Power* 33(9), 2268-2277. (in Chinese)

Lederer, R. (1996). Testing the Actively Cooled, Fully Variable Hypersonic Demonstrator Nozzle. *AIAA* 96-4550.

Lu, X., L. J. Yue, Y. B. Xiao and X. Y. Zhang (2010). Design of three-dimensional section controllable scramjet nozzle. In *The second national hypersonic science and Technology Academic Conference*. Wuxi, Jiangsu Province, China (in Chinese).

Lv, Z., J. L. Xu and J. W. Mo (2017a). Design and analysis on three-dimensional scramjet nozzles with shape transition. *Aerospace Science and Technology* 71, 189-200.

Lv, Z., J. L. Xu and J. W. Mo (2017b). Numerical investigation of improving the performance of a single expansion ramp nozzle at off-design conditions by secondary injection. *Acta Astronautica* 133, 233-243.

Lv, Z., J. L. Xu and J. W. Mo (2017c). Design of a three-dimensional scramjet nozzle considering lateral expansion and geometric constraints. *Acta Astronautica*. 141,172-182.

Melvin, J. B. and S. Adam (2006). The rebirth of round hypersonic propulsion. In *42nd AIAA/ASME/SAE/ASEE Joint Propulsion Conference & Exhibit*, Sacramento, California.

Melvin, J. B. and S. Adam (2011). Combined cycle propulsion: Aerojet innovations for practical hypersonic vehicles. In *17th AIAA International Space Planes and Hypersonic Systems and Technologies Conference*, San Francisco, California.

Siebenhaar, A. and T. Bogar (2006). The impact of round combustors on TBCC propulsion and hypersonic cruise vehicles. In *14th AIAA/AHI Space Planes and Hypersonic Systems and Technologies Conference*, Reston.

Tsunoda, K., T. Suzuki and T. Asai (2000). Improvement of the performance of a supersonic nozzle by riblets. *Journal of Fluids Engineering* 122(3), 585-591.

Waithe, K. and K. Deere (2003). An experimental and computational investigation of multiple injection ports in a convergent-divergent nozzle for fluidic thrust vectoring. In *21st AIAA applied aerodynamics conference*, Orlando, Florida.

Walker, S., F. Rodgers, A. Paull and D. M. V. Wie (2008). Hycause flight test program. In *15th AIAA International Space Planes and Hypersonic Systems and Technologies Conference*, Dayton, Ohio.

Xu, B. C., J. L. Xu, X. Wang, W. Zhu and Y. F. Niu (2017). Flowfield and performance analysis of a three-dimensional tbcc exhaust nozzle. *Journal of Engineering for Gas Turbines and Power* 139(11).

Xu, J. L., Sha, J., J. W. MO, Y. Yu and K. Y. Zhang (2010). Numerical study of improving the performance of the overexpanded sern by using sja. In *46th AIAA/ASME/SAE/ASEE Joint Propulsion Conference & Exhibit*, Nashville, TN.

Zhang, L. H., J. L. Xu and J. W. Mo (2013). Experimental study of 2D adjustable asymmetric nozzles. *Acta Aeronautica Et Astronautica Sinica* 34 (4), 772-778.

Zhou, L. and Z. X. Wang (2019). Numerical investigation on the three-dimensional flowfield in the single expansion ramp nozzle with passive cavity flow control. *Journal of Applied Fluid Mechanics* 12(4), 1115-1126.

Zhou, L., Z. W. Liu, Z. X. Wang and H. Xiao (2016). Numerical study of passive cavity control on high-pressure ratio single expansion ramp nozzle under over-expansion condition. *Proceedings of the Institution of Mechanical Engineers, Part G: Journal of Aerospace Engineering* 230(8), 1409-1422.